Spatial sampling of the thermospheric vertical wind field at auroral latitudes

C. Anderson,[1] T. Davies,[2] M. Conde,[1] P. Dyson,[2] and M. J. Kosch[3]

Received 19 January 2010; revised 8 March 2011; accepted 5 April 2011; published 30 June 2011.

[1] Results are presented from two nights of bistatic Doppler measurements of neutral thermospheric winds using Fabry-Perot spectrometers at Mawson and Davis stations in Antarctica. A scanning Doppler imager (SDI) at Mawson and a narrow-field Fabry-Perot spectrometer (FPS) at Davis have been used to estimate the vertical wind at three locations along the great circle joining the two stations, in addition to the vertical wind routinely observed above each station. These data were obtained from observations of the 630.0 nm airglow line of atomic oxygen, at a nominal altitude of 240 km. Low-resolution all-sky images produced by the Mawson SDI have been used to relate disturbances in the measured vertical wind field to auroral activity and divergence in the horizontal wind field. Correlated vertical wind responses were observed on a range of horizontal scales from ~150 to 480 km. In general, the behavior of the vertical wind was in agreement with earlier studies, with strong upward winds observed poleward of the optical aurora and sustained, though weak, downward winds observed early in the night. The relation between vertical wind and horizontal divergence was seen to follow the general trend predicted by Burnside et al. (1981), whereby upward vertical winds were associated with positive divergence and vice versa; however, a scale height approximately 3–4 times greater than that modeled by NRLMSISE-00 was required to best fit the data using this relation.

Citation: Anderson, C., T. Davies, M. Conde, P. Dyson, and M. J. Kosch (2011), Spatial sampling of the thermospheric vertical wind field at auroral latitudes, *J. Geophys. Res.*, *116*, A06320, doi:10.1029/2011JA016485.

1. Introduction

[2] Vertical winds play an important role in the dynamics of the thermosphere, as these motions can oppose diffusive separation [*Rishbeth et al.*, 1987], resulting in compositional changes, which can in turn affect the thermospheric heating budget [*Smith*, 2000]. On a global scale, vertical winds are assumed to be relatively unimportant, driven predominantly by solar heating of the sunlit atmosphere, which results in a diurnal expansion and contraction of the entire atmosphere, and vertical winds of at most a few m s^{-1} [*Smith*, 1998]. *Conde and Dyson* [1995b], for example, reported a diurnal vertical wind variation of −2.6 to 3.0 m s^{-1} at Mawson station, under low levels of geomagnetic activity. At high latitudes, Joule heating by ionospheric currents and particle heating from auroral precipitation provide spatially localized sources of heat to the lower thermosphere, which are capable of driving stronger and more variable vertical wind activity in the upper thermosphere [*Smith and Hernandez*, 1995]. Many authors have reported high-latitude vertical winds at speeds near or exceeding 100 m s^{-1} [e.g., *Spencer et al.*, 1982; *Wardill and Jacka*, 1986; *Smith and Hernandez*, 1995; *Innis et al.*, 1996, 1999; *Innis and Conde*, 2002].

[3] From a single station, ground-based vertical wind observations are limited to the zenith viewing direction. The time evolution of the vertical wind measured in this way will reflect both changes occurring temporally, due to localized, rapidly time-varying energy inputs, and spatially, as the station is carried along with Earth's rotation into regions (in a Sun-aligned coordinate frame) of quasi-stationary forcing associated with geomagnetic energy/momentum sources [*Rees et al.*, 1984]. Satellites allow for vertical wind measurement along the orbital track, but such measurements essentially provide a "snapshot" of the vertical wind field at one time, without following the temporal evolution of this field.

[4] In a bistatic experiment, two ground-based spectrometers are employed to observe the region of overlap of their individual fields of view (the "common volume" region). Each instrument returns an estimate of the radial line-of-sight wind from multiple small regions within the common volume. By combining the estimates from each instrument within the same (small) observing volume, it is possible to determine unambiguously two of the three vector components of the wind field, specifically those components lying in the plane which intercepts both stations and the volume being observed. In the special case of common volume regions lying along the line (great circle) joining the

[1]Geophysical Institute, University of Alaska Fairbanks, Fairbanks, Alaska, USA.
[2]Department of Physics, La Trobe University, Melbourne, Victoria, Australia.
[3]Department of Physics, Lancaster University, Lancaster, UK.

0148-0227/11/2011JA016485

two stations, these components are the vertical wind and the component of the horizontal wind in the plane of the great circle. By observing multiple points along the direction of this line, both the spatial variation and temporal evolution of the vertical wind field may be investigated.

[5] Bistatic investigations of vertical wind at midlatitude have been carried out by *Sipler et al.* [1995]. These authors observed larger than expected vertical winds on geomagnetically quiet nights and strong downward wind (<-50 m s^{-1}) during one magnetically disturbed period ($7 \leq Kp \leq 8$). An average of three geomagnetically disturbed nights showed a significant vertical wind variation throughout the night. At high latitudes, tristatic Fabry-Perot interferometer studies have been reported by *Aruliah et al.* [2004, 2005], which demonstrated mesoscale variability of the horizontal neutral wind and temperature; however, neutral vertical winds were not presented.

[6] In this article, results are presented from a campaign of bistatic observations of thermospheric neutral winds between two Fabry-Perot spectrometers located at Mawson (67°36′S, 62°52′E, Inv 70°30′S) and Davis (68°35′S, 77°58′E, Inv 74°36′S) stations in Antarctica. These instruments measured winds by observing Doppler shifts of the 630.0 nm airglow line of atomic oxygen, which has a peak emission altitude of approximately 240 km.

2. Instrumentation

2.1. Mawson SDI

[7] The Mawson Scanning Doppler Imager (Mawson SDI) has been described previously [*Anderson et al.*, 2009]. This instrument is of the type described by *Conde and Smith* [1997]. It is capable of acquiring spectra at many tens of locations (referred to as "zones") simultaneously across an approximately 144° full-angle field of view of the sky. Measurements of Doppler shift of the 630.0 nm airglow emission of atomic oxygen in each zone were converted into line-of-sight wind speed, from which an estimate of the two-dimensional horizontal vector wind field was obtained using the method of *Conde and Smith* [1998]. In addition to, and concurrently with, spectral acquisition, the SDI is able to generate a low-resolution, spectrally unmodulated, monochromatic image of the sky at the same wavelength as the spectra and over an identical field of view. These all-sky images are useful for relating structures in the wind and temperature fields to auroral features in the sky.

2.2. Davis FPS

[8] The Davis Fabry-Perot spectrometer (Davis FPS) is a narrow-field instrument which uses a periscope to accept light from an approximately 6° full-angle field of view of the sky. The periscope actually consists of two tubes which are directed along azimuths separated by 180°. Mirrors beneath each tube direct light toward a central mirror, which is rotated to select light from one of these two tubes. This allows the instrument to observe opposite parts of the sky at the same zenith angle without having to rotate the periscope, improving time resolution. Light collected by the periscope is directed through a 130 mm (working diameter) fixed-gap Fabry-Perot etalon, before it is focused by a 150 mm diameter fringe-forming lens onto a third generation Gallium Arsenide image intensifier. An image of the interference fringes, containing one complete fringe and a fraction of a second, is recorded by a Pulnix CCD camera (768 × 576 pixels). Camera exposure times are dynamically selected by the control software in order to maintain a sufficiently high signal-to-noise ratio. Typical exposure times vary from approximately 15 s during very active aurora to around 200 s when signal levels are low.

[9] In routine operation the Davis FPS observes in the geographic cardinal directions (north, south, east, and west at a zenith angle of 30°) and also in the zenith. Upon completion of this sequence of sky observations the periscope is directed downward toward an opal glass screen which is illuminated by a frequency-stabilized He-Ne laser, and a calibration fringe image is recorded, after which the observing cycle repeats. In late 2007, four additional look directions were included in the cycle of sky observations, which directed the periscope along a bearing of 87° west of geographic north (the bearing of the Davis-Mawson great circle), at zenith angles of 35°, 55°, 66°, and 72.5°. These look directions intersect the airglow layer in volumes which are common to both the Mawson and Davis instruments and are located along the direction of the great circle between the two stations.

[10] An interference fringe image was recorded by the Davis FPS for each observing direction. Spectral information is encoded in the spatial variation of light intensity across the two-dimensional fringe image. Following *Conde* [2002], wavelength spectra were derived by fitting model interference fringes to the observed laser calibration fringes. Model fringes defined the spatial variation of interference order across the corresponding laser fringe image and therefore defined the spectral channel to which each pixel in the image would contribute. Spectra were derived by adding the digital number recorded at each pixel to the appropriate spectral channel (covering one free spectral range of the etalon). For the data presented here each spectrum contained 64 channels, spanning a wavelength range of 15.3 pm.

[11] This method of reducing two-dimensional fringe images to one-dimensional wavelength spectra has the advantage that noncircular fringes do not broaden the derived spectra, since departures from perfect circularity are accounted for by changing the shape of the model fringe to fit the observed laser fringes. Parameters that define the shape of the model fringes vary slowly throughout the night (these variations are very small) and were linearly interpolated in time to give model fringes that were applicable to the times at which airglow fringe images were available.

3. Analysis

[12] For both instruments the raw data consisted of wavelength spectra of the λ630.0 nm airglow line of atomic oxygen. Calibration spectra derived from viewing He-Ne frequency-stabilized lasers (λ632.8 nm) were used to measure the instrument function and track instrumental drift. The measured instrument function was convolved with a Gaussian emission profile and least squares fitted to the recorded airglow spectrum to yield best estimates of peak wavelength (relative to the first laser peak wavelength), temperature, emission intensity, and continuum background. The spectral fitting algorithm employed in this study is described by *Conde* [2001]. Instrumental drift on each night

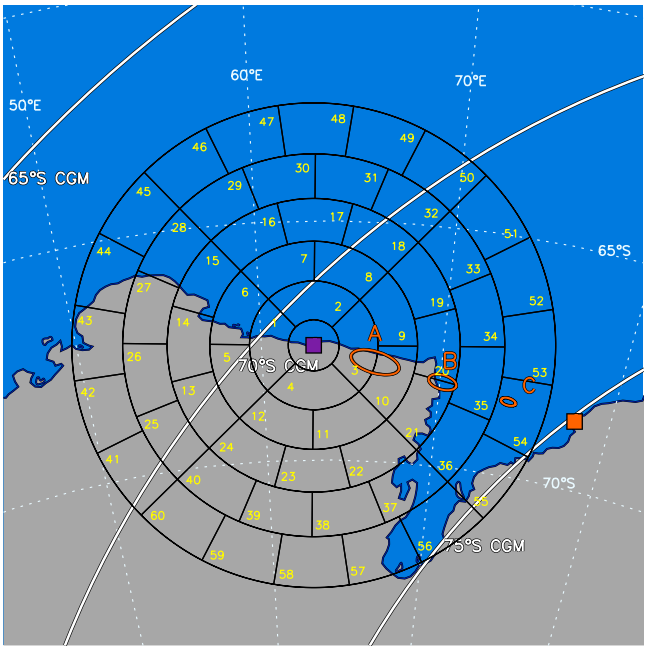

Figure 1. Common volume viewing geometry. Mawson (purple square) and Davis (orange square) are shown, along with Mawson SDI viewing zones (numbered sectors, outlined in black) and Davis look directions (orange ellipses). The grey area is the Antarctic continental land area, whereas the blue area indicates the southern ocean.

was tracked by monitoring the change in peak wavelength of the calibration spectra relative to the first calibration peak wavelength of the night. This drift was interpolated to the times at which airglow exposures were made and subtracted from the airglow peak wavelength time series. Using the assumption of zero net vertical wind over the course of the night [see, e.g., *Aruliah and Rees*, 1995], the median zenith-looking peak wavelength (over the entire night) was used as a zero-velocity reference. Line-of-sight wind speeds in all look directions were then calculated relative to this zero-velocity reference.

[13] The locations of the Mawson SDI and Davis FPS are shown in Figure 1. In Figure 1 the Mawson SDI is indicated by the purple square, and the SDI viewing zones are the numbered sectors. The orange square marks the location of the Davis FPS, while the Davis common volume look directions are shown by orange ellipses. The three common volume regions used in this study will henceforth be referred to as regions A, B, and C, and the details of the Mawson and Davis look directions for each of these regions are given in Table 1.

Table 1. Common Volume Look Directions

	Volume		
	A	B	C
Davis zenith angle	66°	55°	35°
Davis bearing	N87°W	N87°W	N87°W
Distance from Davis (km)	480	318	160
Mawson zenith angle(s)	23.76°, 39.96°	51.84°, 51.84°	66.96°
Mawson bearing(s)	N91°E, N113.5°E	N91°E, N121°E	N109°E
Mawson zone(s)	3, 10	20, 21	54
Distance from Mawson (km)	142	286	498

[14] The geometry of an arbitrary common volume observation is shown in Figure 2. The positive x axis has been chosen to point in the direction from Mawson to Davis, and vertical wind is positive upward. Purple and orange arrows show respectively the Mawson and Davis line-of-sight wind speed estimates, labeled v_m and v_d. If $\hat{\mathbf{m}}$ and $\hat{\mathbf{d}}$ are used to denote the unit vectors along the lines of sight of the Mawson and Davis observations, respectively, and the true wind vector in the common volume is $\mathbf{v}$, then we have:

$$v_m = \mathbf{v} \cdot \hat{\mathbf{m}} = v_x m_x + v_z m_z \quad (1)$$

$$v_d = \mathbf{v} \cdot \hat{\mathbf{d}} = v_x d_x + v_z d_z \quad (2)$$

Equations (1) and (2) can be written in the form of a matrix equation:

$$\begin{bmatrix} v_m \\ v_d \end{bmatrix} = \begin{bmatrix} m_x & m_z \\ d_x & d_z \end{bmatrix} \begin{bmatrix} v_x \\ v_z \end{bmatrix} \quad (3)$$

The 2 × 2 matrix in equation (3) contains the components of the unit vectors along the lines of sight from Mawson and Davis to the common volume point. For volumes lying between Mawson and Davis, these components are given in terms of the zenith angles of the look directions from each station, θ_m and θ_d. Equation (3) can then be solved to give the components of the two-dimensional vector along the $\hat{\mathbf{x}}$ and $\hat{\mathbf{z}}$ directions:

$$\begin{bmatrix} v_x \\ v_z \end{bmatrix} = \begin{bmatrix} \sin(\theta_m) & \cos(\theta_m) \\ -\sin(\theta_d) & \cos(\theta_d) \end{bmatrix}^{-1} \begin{bmatrix} v_m \\ v_d \end{bmatrix} \quad (4)$$

These components, along with the full two-dimensional vector, are shown as dark green arrows in Figure 2. As a result of this geometry a purely vertical wind in the common volume will result in line of sight wind estimates which are positively correlated between the two stations, while a

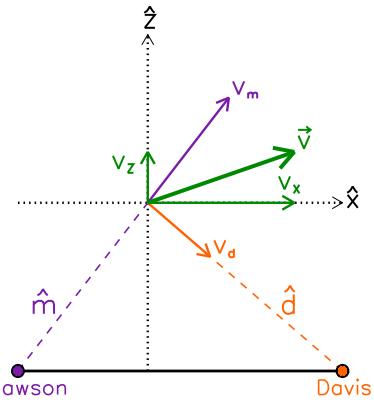

Figure 2. Geometry of an arbitrary common volume wind measurement. The true wind vector (green) is estimated by viewing along the Mawson (purple) and Davis (orange) lines of sight.

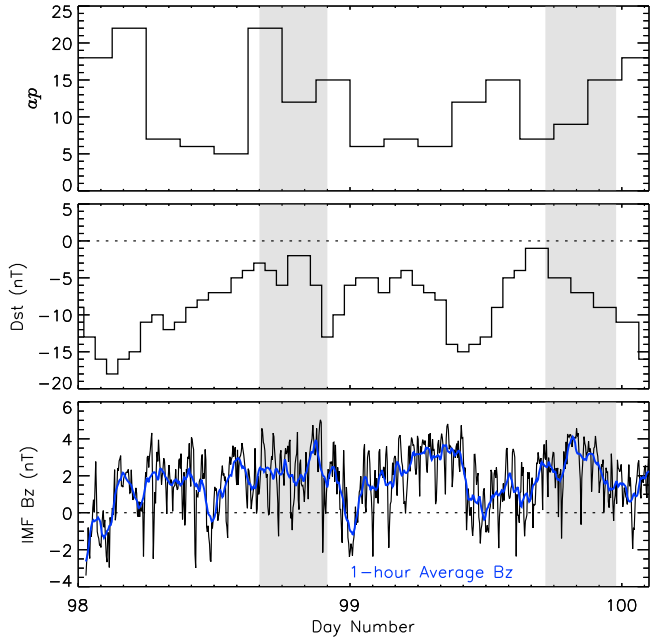

Figure 3. Geomagnetic and IMF conditions during the study periods (grey shaded regions).

purely horizontal wind will produce line-of-sight wind estimates at each station which are anticorrelated.

[15] For a given common volume region, each instrument measured line-of-sight wind speed with a different time resolution. The Davis FPS, which needed to reposition its periscope after each common volume observation, typically generated data with a lower time resolution than did the Mawson SDI, which was able to record data from all its look directions (zones) simultaneously. As such, to make full use of the available data, observations from both instruments were interpolated to a set of "common times", defined by the union of the sets of observation times from each station. That is, any (universal) time at which an observation was made from either station became a common observation time. The set of all such times formed a new sample grid of universal times, to which the observations from both instruments were linearly interpolated. As a result, the high-frequency (<10 min) variations observed in the derived common volume vertical wind were due primarily to variations in the data recorded by the Mawson SDI. This is considered acceptable, as observations from Mawson at multiple zenith-angles have shown that the high-frequency component of the measured line-of-sight wind is predominantly due to the vertical wind contribution.

[16] This does, however, mean that the magnitude of the high-frequency component of the vertical winds inferred in the common volume regions were (in general) underestimated by this technique. Consider the effect on the measured line-of-sight wind estimates of a purely vertical wind event in the common volume region. If both instruments were able to resolve this event (in time), then the line-of-sight wind estimates would show a correlated deviation in response to the vertical wind (the magnitude of the deviation would depend on each instrument's viewing zenith angle). However, if only one instrument resolved the deviation, then the bistatic inversion would produce a solution consistent with this, namely one with a nonzero horizontal component. The magnitude of the inferred vertical wind would thus be underestimated (and the magnitude of the horizontal component overestimated). Thus the high-frequency fluctuations in the inferred common volume vertical winds were in general underestimated in the present study.

4. Results

[17] Results from two consecutive nights, 7 and 8 April 2008, are presented. These nights will be referred to by day number, days 98 and 99, respectively. Geomagnetic and Interplanetary Magnetic Field (IMF) conditions throughout the period are shown in Figure 3, with the observation times for the two study intervals shaded in grey. From the top are displayed the 3-h *ap* index, D_{st} index, and the Bz component of the IMF as measured by the ACE satellite (4-min and 1-h average), delayed by (on average) 40 min to account for the satellite position. In terms of solar and geomagnetic activity 2008 was an extremely quiet year on average and this is reflected in Figure 3. The period was characterized by a predominantly northward IMF of low ($\leq$ 5 nT) magnitude. Three-hourly *ap* reached a maximum of 22 at the beginning of the study interval for day 98; however, it had remained low ($\leq$7) during the approximately 10 h preceding observations on that night. On day 99 *ap* increased steadily during the observation period from 6 to 18. D_{st} was continuously negative and of small magnitude ($|D_{st}| < 15$ nT) during both study intervals.

[18] The line-of-sight wind speed and normalized emission intensity estimates from each instrument are shown for each study interval in Figures 4–5, wind estimates on the left and emission intensity on the right. In Figures 4–5, wind estimates from the Mawson SDI are shown in blue, those from the Davis FPS are shown in red, and the measurement

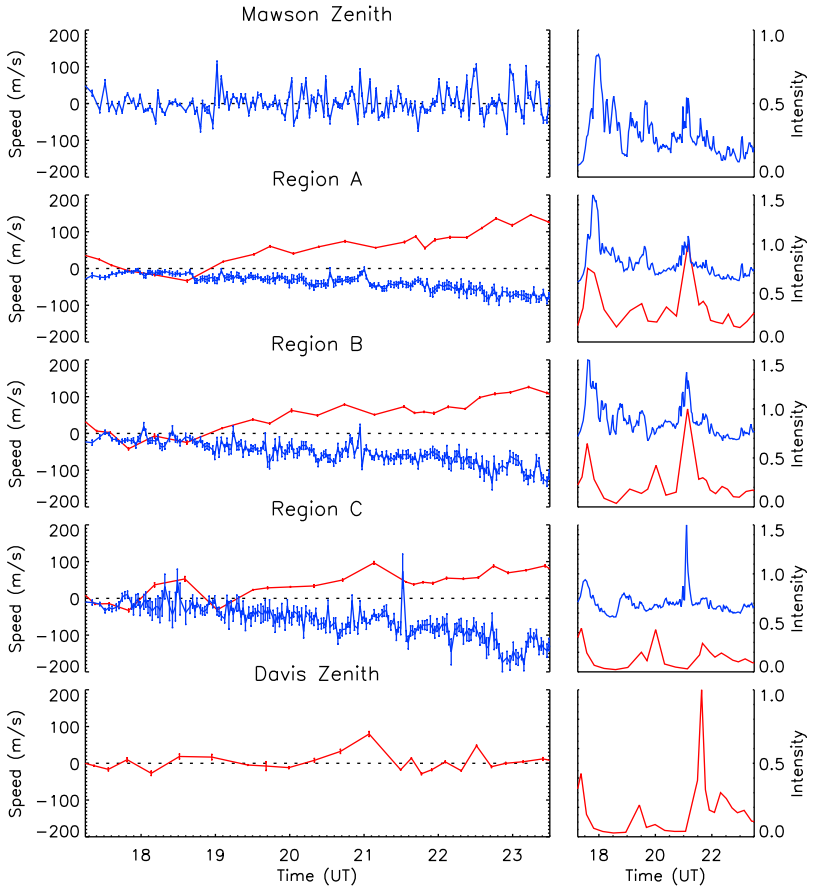

Figure 4. Line-of-sight wind estimates from Mawson (blue) and Davis (red) in each of the common volume regions and in the local instrument zenith, for 8 April 2008, day 99. Error bars show the 1σ uncertainties in the wind estimates. Times of Davis data have been adjusted as described in the text.

volumes are plotted from top to bottom in order of increasing distance from Mawson, starting in the Mawson zenith. Shown at the top and bottom are the local vertical wind and emission intensity measured in the station zeniths. Error bars are used to indicate the 1σ uncertainty in the measured wind speeds. Intensities are normalized to aid comparison between the two instruments, which are not calibrated to measure absolute intensities (in Rayleigh for example). In each of the common volume regions the intensity estimates from the Mawson SDI (blue) have been offset by +0.5 for clarity.

[19] Comparison between the emission intensity estimates in the common volume regions during the initial analysis revealed a consistent, though small, time offset between the two instruments, which was later attributed to a computer clock synchronization problem at Davis. Each instrument records the column-integrated intensity along its own measurement line of sight, and thus differences in recorded intensity, even when viewing the same nominal volume, can and will occur between the two instruments due to their different lines of sight. However, such differences are unlikely to be consistent across many nights as was observed. Since a consistent time offset was observed, this was most likely due to a clock error. Thus in order to maximize the correlation between intensities measured in the common volume regions, the data from the Davis FPS have been shifted forward in time by 12 min.

[20] Figures 4 and 5 (left) show a slowly time-varying trend of anticorrelated line-of-sight wind estimates from each station in the common volume regions A, B, and C. This trend indicates that the component of the horizontal wind parallel to the Mawson-Davis great circle was steadily increasing throughout both nights. The Mawson-to-Davis bearing is approximately 30° east of the corrected geomagnetic (CGM) south direction from Mawson; thus the Mawson-Davis great circle direction is close to being geomagnetically north-south aligned. The common volume observations therefore indicated an increasing magnetic meridional wind throughout both nights, consistent with the horizontal wind flow estimated by each instrument individually (see Figure 9 (top) for Mawson SDI horizontal winds) and also with previous observations above Mawson [*Jones et al.*, 1987; *Conde and Dyson*, 1995a; *Smith et al.*, 1998; *Greet et al.*, 1999; *Anderson et al.*, 2009].

[21] The vertical wind derived in each of the common volume regions is shown in Figures 6 and 7 for days 99 and 98, respectively. The winds are again plotted from top to bottom in order of increasing distance from the Mawson zenith. In the common volume regions the error bars indicate the uncertainties in the derived vertical wind estimates, calculated from the 1σ uncertainties in the underlying line-

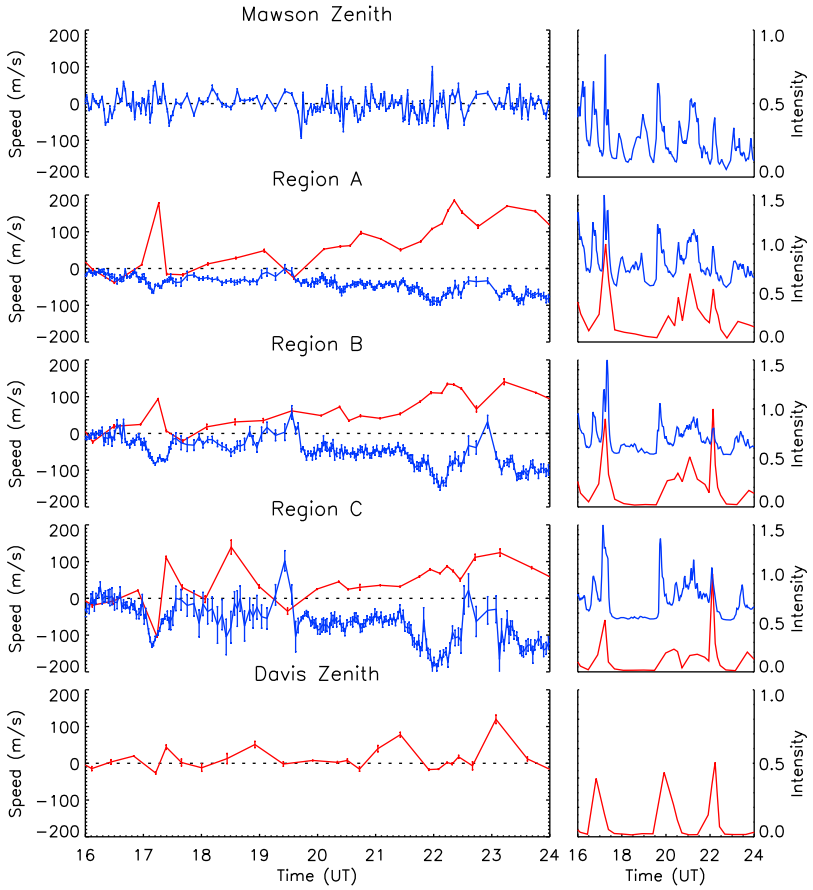

Figure 5. Same as Figure 4 except for 7 April 2008, day 98.

of-sight wind data. Beneath the vertical winds is shown a keogram derived from vertical cross sections through each Mawson SDI all-sky image (taken along the corrected geomagnetic north-south meridian) plotted as a function of universal time. Each all-sky image was scaled and smoothed with a two-point boxcar average before the vertical cross section through the middle of the image (pixel "x" coordinate 256) was extracted. The ordinate of the keogram corresponds to projected latitude (at an altitude of 240 km) with geomagnetic north at the top (note that this is not exactly equivalent to a slice along the great circle direction between the two stations). Figures 6 and 7 are plotted against a common universal time axis, which is shown underneath the keogram. Each day is discussed in detail below.

4.1. Day 99

[22] Day 99 (Figure 6) is discussed first as this day demonstrates the viability of the technique on a night that showed relatively minor vertical wind disturbance. Variability above Mawson was significant, where vertical wind speeds >50 m s^{-1} were frequently observed. Prior to 19:00 UT a downward wind of 40–50 m s^{-1} was observed in regions A and B. During this period of downward wind in regions A and B a sinusoidal variation of ~30 m s^{-1} amplitude was observed in region C, which began as a downward wind (at the start of observations) before it reversed direction at 18:00 UT to become an upward wind, then reversed a second time at 18:50 UT to become downward once again. Each upward/downward wind lasted for approximately 40–50 min, and the disturbance had abated by 19:30 UT. The variability above Mawson meant that no clear signature of a downward wind was observed there similar to that in region A, however the direction of the vertical wind during the period prior to 19:00 UT was more often downward than upward.

[23] After 18:00 UT the aurora had reached its furthest northward position and remained approximately 2° magnetically northward of the Mawson zenith until it began to decrease in brightness around 18:40 UT. In region C the upward wind between 18:00 and 18:50 UT occurred as the auroral brightness decreased significantly in the region, while each period of downward wind was observed when the intensity in the region was marginally higher. The larger vertical wind uncertainties in region C during the upward wind resulted directly from the lower intensity, which reduced the spectral signal-to-noise ratio and consequently increased uncertainty in the spectral fits. However, the vertical winds observed during the event were frequently larger than the 1σ uncertainty.

[24] A second period of disturbance was observed to coincide with a significant brightening and latitudinal expansion of the aurora equatorward of Mawson around 20:40 UT. In the Davis zenith an upward wind was observed which reached a peak speed of 80 m s^{-1} at 21:05 UT. A similar upward wind was observed concurrently in region C,

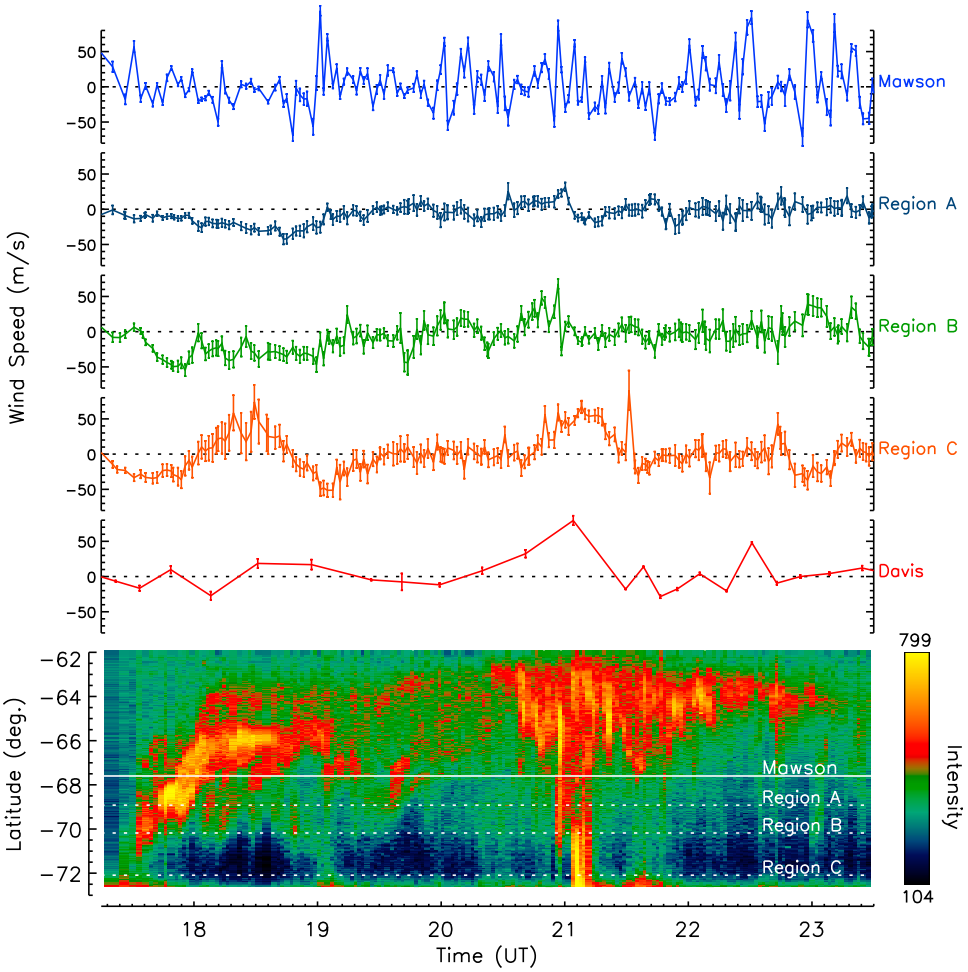

Figure 6. (top) Vertical winds above each station and derived in the common volume regions on 8 April 2008, day 99. (bottom) Keogram derived from the Mawson all-sky images. The approximate latitudes of the common volume regions and of Mawson station are indicated on the keogram by horizontal lines, and the intensity scale is shown on the right (arbitrary units).

where the peak speed was closer to 60 m s^{-1}. In regions A and B it appeared that only the beginning of this disturbance was observed, as upward winds increased while the aurora brightened and expanded latitudinally; however, in both regions the upward motions ended abruptly at approximately 21:00 UT, just as the region of auroral brightness had expanded to cover those regions. In region A following the abatement of the upward wind a period of weak (~20 m s^{-1}) downward wind was observed which lasted until the end of the period of upwelling in region C (at approximately 21:30 UT). Above Mawson the large variability again made it difficult to discern any consistent vertical motion during the period 20:40–21:30 UT. Following the upward wind in region C, a strong vertical wind spike of around 100 m s^{-1} was observed, which was not seen concurrently in any other region.

[25] One final event worth noting on day 99 was associated with the fading of the aurora around 22:50 UT, which had previously been brightest equatorward of Mawson. Region C observed a ~30 m s^{-1} downward wind while an upward wind of similar magnitude was observed concurrently in region B. No signature of this vertical wind event was seen in region A or above Davis.

4.2. Day 98

[26] Despite the similarity in geomagnetic conditions between the two study intervals (*ap* reached slightly higher levels on day 98) the night of 7 April, day 98 (Figure 7) showed much stronger vertical wind disturbance in the common volume regions than was observed on day 99. Auroral brightness was generally higher on day 98, and the auroral forms often more localized latitudinally. The first period of interest began with a moderate 40–50 m s^{-1} downward wind in region A which peaked at 16:30 UT, at which time a discrete auroral arc was moving equatorward through the Mawson field of view. Downward vertical winds were observed above Mawson during this time, although not as consistently as in region A and upward winds were also observed. The region A downward wind decreased steadily in magnitude between 16:30 and 17:10 UT and then accelerated in the upward direction over the next ~5 min to reach a peak upward speed of 50 m s^{-1} at

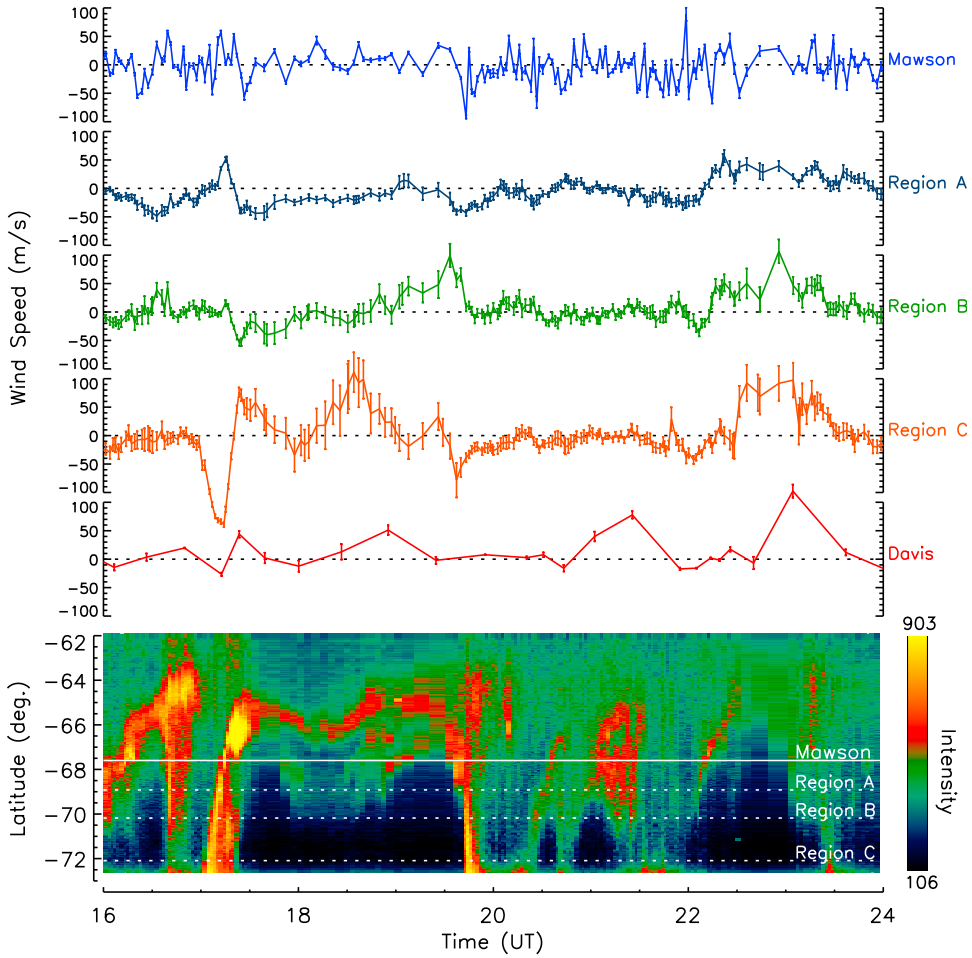

Figure 7. Same as Figure 6 except for 7 April 2008, day 98. Note the larger vertical wind scale compared to Figure 6.

17:15 UT. After the peak the upward wind rapidly abated and became a downward wind approximately 5 min after the peak in upward speed and reached a maximum downward speed of 44 m s^{-1} around 17:35 UT. There followed a very gradual abatement of this wind over the next 1–1.5 h.

[27] Concurrently with the change from upward to downward wind in region A (17:20 UT) a downward wind was observed to begin in region B. This wind was very similar to that seen in nearby region A, although a slightly larger maximum downward wind speed of 54 m s^{-1} was reached in region B. The downward wind in region B abated more quickly than that in region A, reaching ~0 m s^{-1} around 18:10 UT. By far the largest response to this disturbance was observed in region C, where a strong downward wind was observed to begin as the auroral arc which had been equatorward of the Mawson zenith abruptly disappeared and was replaced by an arc at the poleward edge of the Mawson field of view. The peak of the downward wind, which occurred at approximately the same time as the peak of the region A upward wind (17:15 UT), reached a maximum speed of −158 m s^{-1}, before reversing direction (concurrently with the direction reversal in region A) and reaching a maximum upward speed of 75 m s^{-1}. After the peak upward wind speed there followed an abatement which occurred over the same timescale as that in region B. A similar vertical wind variation as that seen in region C was observed concurrently above Davis, however the speeds reached were smaller, with downward/upward winds of ~30/40 m s^{-1}. The abatement above Davis was correspondingly faster.

[28] This initial disturbance coincided with rapid evolution of auroral morphology, beginning with the disappearance of a predominantly equatorward auroral arc and the fast equatorward motion of an arc which replaced it on the poleward edge of the Mawson SDI field of view. The strong downward wind in region C was observed to begin as the equatorward arc disappeared, and both the region A upward wind and region C downward wind peaked as the keogram showed aurora covering all latitudes between region C and the Mawson zenith. Figure 8 gives a detailed view of the evolution of the aurora and the horizontal wind field during this disturbance between 16:53 and 18:02 UT. Shown in Figure 8 are single exposures of the Mawson SDI (displayed at approximately half the available time resolution), showing the geographically mapped all-sky image (false color) and fitted vector wind field (green arrows) in relation to the Antarctic coastline. The zones corresponding to the common volume regions are outlined in white and Mawson and

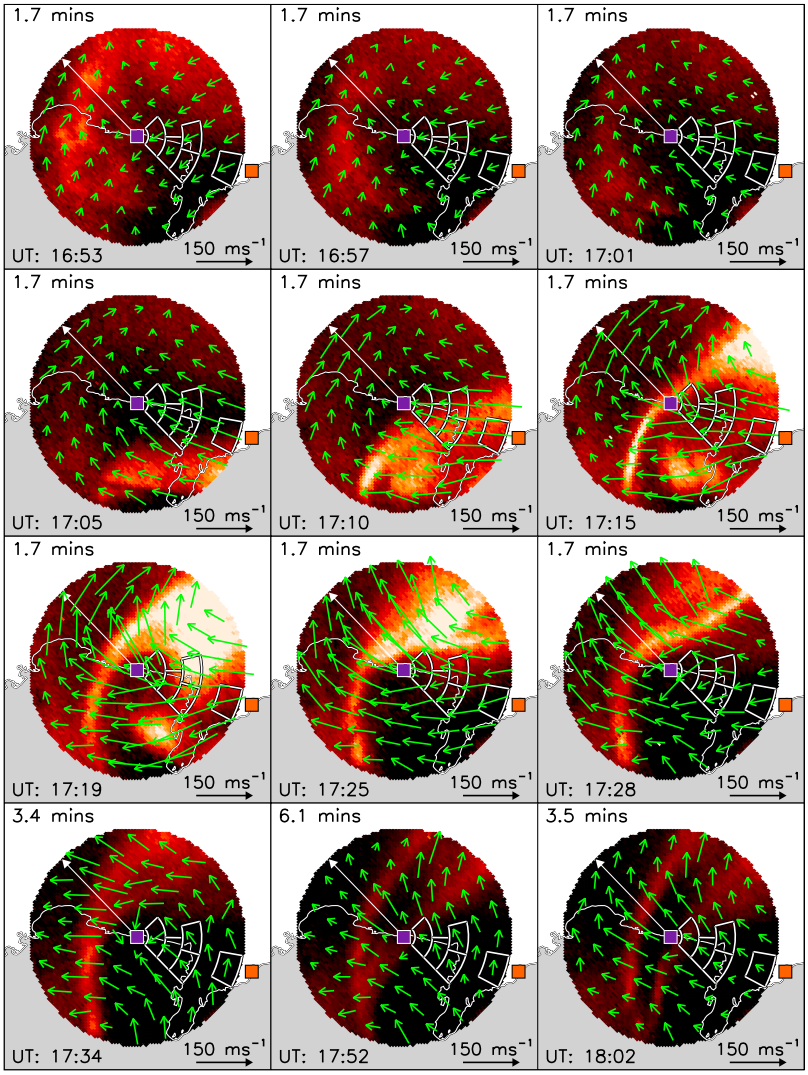

Figure 8. Evolution of auroral morphology and the thermospheric wind field on 7 April 2008, day 98. Geographically projected all-sky images (false color) from the Mawson SDI are shown overlaid on maps of the Antarctic continent (grey area) and southern ocean (white area). Green arrows show the inferred horizontal wind field; the white arrow from the center to the edge of the field of view indicates the geomagnetic north direction. Mawson and Davis stations are indicated by purple and orange squares, respectively, and the white annular segments correspond to the Mawson zones in regions A, B, and C. The universal time at which each exposure was made is shown in the bottom left corners, with the exposure time (in minutes) shown in the top left corner. The vector wind scale is shown in the bottom right corner.

Davis stations are indicated by purple and orange squares, respectively. Also shown are the central time of the exposure and the integration time in seconds. The white arrow from the center to the edge of the Mawson SDI field of view indicates the geomagnetic north direction. The following discussion assumes a geomagnetic coordinate frame.

[29] Figure 8 reveals detailed auroral structure which was not apparent in the keogram, namely a loop-like auroral form which moved rapidly northward through the field of view, bringing with it dramatic changes in the inferred horizontal wind field. For approximately 40 min prior to the appearance of this arc the median horizontal wind speed across all zones was extremely low, $\leq$25 m s^{-1}. As the arc swept northward it brought with it an explosive increase in wind speed, such that a strong wind gradient was apparent on the equatorward edge of the arc as the region of faster flow crossed into the previously stagnant wind field. Approximately 20 min after the arc appeared the median horizontal wind speed across all zones had increased to 110 m s^{-1}. Horizontal winds collocated with the arc were initially directed geomagnetically northwestward (17:10 UT), with a latitudinally narrow region of eastward flow at the northern edge of the field of view. As the arc progressed northward, the winds collocated with the northward edge of the arc acquired this eastward component, while winds to the geomagnetic south continued northwestward. Divergence was apparent near the Mawson zenith between 17:15 and 17:25 UT, with convergence on the northward edge of the arc. By approximately 17:30 UT, the arc had reached its farthest northward position and subsequently began to decrease in

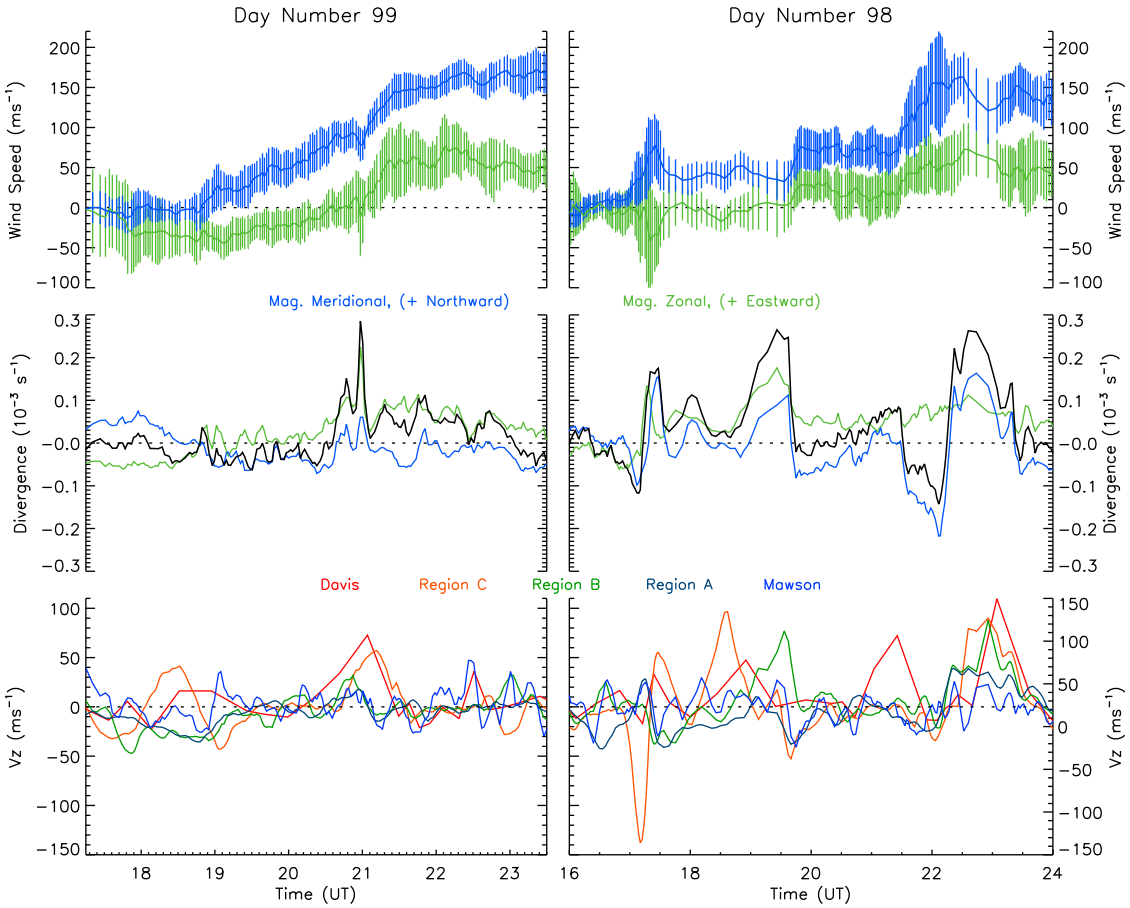

Figure 9. (top) Average magnetic meridional wind (blue) and magnetic zonal wind (green) as measured by the Mawson SDI for days (left) 99 and (right) 98. Error bars show the 1σ spread in each component across all Mawson SDI viewing zones. (middle) Magnetic meridional (blue) magnetic zonal (green) and total (black) divergence of the vector wind field fitted to the Mawson SDI line-of-sight wind data, for the corresponding day shown at the top. (bottom) Ten-minute smoothed station zenith and common volume vertical winds, superposed for comparison.

brightness over the next ~30 min, leaving a weaker wind field (median speed ~50 m s^{-1}) directed predominantly geomagnetically northward.

[30] The peaks of the Davis/region C downward wind and region A upward wind were observed as the northward arc of the aurora was located in the Mawson zenith (17:15 UT), while in the common volume regions there was relatively less auroral brightness. The vertical wind direction reversals in regions A and C and in the Davis zenith (and the beginning of the region B downward wind) occurred 5 min later, as the northward motion of the auroral arc brought the southeastern part of the arc into the common volume regions, and the discrete northern edge of the arc moved northward of the Mawson zenith. The rate at which the disturbance abated in each region appeared to depend on the region's distance from the northernmost auroral arc, which was the last part of the auroral form to fade out (not shown in Figure 8). As such the abatement was complete above Davis by 17:40 UT, in region C by 17:53 UT, in region B by 18:10 UT, and lastly in region A by 19:00 UT.

[31] From Figure 8 it is obvious that the horizontal wind field was strongly perturbed by the passage of the auroral arc. The geomagnetic meridional and zonal components of the horizontal wind measured by the Mawson SDI (for both nights) are shown in Figure 9 (top). The median of each component (across all zones) is shown as a thick curve (blue for meridional, green for zonal) with error bars indicating the 1σ spread in each component across all zones. Figure 9 (middle) shows the total horizontal divergence determined from the fitted wind field. The two contributions to the divergence (meridional, blue and zonal, green) are shown, along with the total horizontal divergence (black). The divergence shown in Figure 9 must be considered an average across the Mawson SDI field of view. Figure 9 (bottom) shows the 10-min smoothed vertical winds from the station zeniths and common volumes superposed for comparison.

[32] On day 98 (Figure 9, right) the disturbance which began around 17:00 UT was seen as spikes in the horizontal wind time series, increasing the median magnetic westward and equatorward flows by 30 and 50 m s^{-1}, respectively, above background levels and lasting for approximately 30 min. The spread in wind estimates also increased significantly during this period. The divergence plot showed a peak in convergent flow near 17:09 UT, caused primarily by the passage of the fast flow on the magnetic equatorward edge of the auroral arc into the relatively stagnant background

flow. At approximately 17:12 UT the convergent flow on the equatorward edge of the arc was balanced by the divergent flow nearer the Mawson zenith, reducing the average divergence to near zero. By 17:25 UT divergent flow was dominant, and by 17:39 UT both the divergence and horizontal wind components had returned to their approximate background levels (however the gradients remained variable).

[33] Following the initial disturbance which has been described at length above, some localized upward winds were observed above Davis and in regions C and B. The first was observed in region C, and reached a peak speed of 110 m s^{-1} at 18:34 UT. This was followed closely by a more moderate upward wind above Davis, peaking at 18:55 UT with a speed of ~50 m s^{-1}. Region B observed upward winds which peaked at 19:30 UT with a speed of 100 m s^{-1}, similar to that seen earlier in region C. In region A a downward wind peaked approximately 10 min after the peak of the region B upward wind and reached a speed of −40 m s^{-1}. Above Mawson a 90 m s^{-1} downward wind spike was observed during the region A peak downward wind (~19:40 UT) and despite a subsequent upward wind spike remained downward for approximately the same length of time as did the region A vertical wind. These individual vertical wind events were observed during a period of low intensity as the aurora was located equatorward of Mawson. The region of peak auroral brightness was observed to oscillate in latitude until approximately 19:30 UT when it retreated poleward, leaving most of the field of view filled with only diffuse auroral brightness.

[34] There followed a period of reduced vertical wind activity between ~20:00 and 22:00 UT at all locations except above Davis. Between 21:00 and 21:30 UT, as a patch of enhanced auroral brightness appeared overhead of Mawson, Davis observed an upward wind speed of 78 m s^{-1}, with no disturbance recorded in any other region. The final disturbance of the night began at approximately 22:00 UT, with moderate downward winds in every region lasting ~10 min, followed in all regions (except perhaps in the Mawson zenith) by upward winds which again coincided with exceptionally low auroral brightness in the common volume regions and in the Davis zenith. The peak magnitude reached during the upward winds generally decreased with increasing distance from Davis. Peak speed above Davis was 120 m s^{-1}, 98 m s^{-1} in region C, 105 m s^{-1} in region B, and 57 m s^{-1} in region A. Above Mawson the data were inconclusive; however, the auroral brightness was greatest there during the period. This large-scale upward motion lasted approximately 1 h 35 min and abated as the brightness in each region increased. Figure 9 shows that during this large-scale upward wind event between 22:10 and 23:45 UT the horizontal wind field displayed large horizontal divergence (relative to the magnitudes seen earlier in the night). Prior to this the horizontal wind field was moderately convergent on average, at which time weak downward winds were observed in all regions.

5. Discussion

[35] Investigations of thermospheric vertical winds at auroral latitudes have often been restricted by a lack of information regarding the temporal evolution of the vertical motions at multiple spatial locations. Satellite measurements, for example those made by the Wind and Temperature Spectrometer (WATS) [*Spencer et al.*, 1981] aboard Dynamics Explorer 2 (DE-2), essentially resolve spatial variations but provide little information on temporal evolution. The reverse is true for a single ground-based observatory. The bistatic experiment described above overcomes these limitations by unambiguously solving for the vertical (and one horizontal) component of the wind field at multiple locations and following the temporal evolution of the wind at those locations.

[36] The periods of strongest sustained upward winds from the two nights examined in this study were observed at locations poleward of the auroral oval (for example between 20:40 and 21:30 UT on day 99 and 18:00–19:45 UT and 21:00–23:45 UT on day 98), in agreement with previous studies of vertical winds above Mawson [*Innis et al.*, 1996, 1999] and elsewhere [e.g., *Price et al.*, 1995; *Ishii et al.*, 2001; *Ishii*, 2005]. Sustained, weak downward motions were observed on both nights in some regions prior to ~19:00 UT. This is in qualitative agreement with observations reported by *Greet et al.* [2002], who derived hourly mean vertical winds above Davis and Mawson over 4 years and related these data to the nominal position of the auroral oval. On the poleward edge of the nominal oval, *Greet et al.* [2002] found that downward winds were observed on average in the early magnetic evening, with upward vertical winds near magnetic midnight. *Greet et al.* [2002] also reported that vertical winds observed on the poleward edge of the auroral oval were of larger amplitude than those observed underneath the oval, again consistent with the bistatic results reported here.

[37] The two nights shown in the current work also revealed spatial structure on a range of scales. On day 99 for example sustained downward winds were observed in regions A and B prior to 19:00 UT. The distance between adjacent common volume regions is on the order of 150 km. In region C during this period a downward wind was interrupted by an upward wind for approximately 50 min. Thus between regions A and B there was good correlation over the ~150 km baseline, while region C observed an upward wind which did not appear in adjacent regions (although the decrease in downward wind speed in region B may have been related to this event). At a later time on the same night, between 20:40 and 21:30 UT there was good correlation shown between region C and the Davis zenith when a moderate upward wind was recorded in both regions. The start of this disturbance was also observed in regions A and B, indicating some degree of correlation over ~480 km; however, midway through the disturbance (at approximately 21:00 UT) the correlation was abruptly reduced, with region A recording a weak downward wind and region B showing a complete abatement as the upward winds peaked above Davis and in region C. Also on day 99 anticorrelated vertical winds were observed between regions B and C in conjunction with fading aurora around 22:50 UT.

[38] On day 98 during the initial disturbance between ~16:30 and 18:00 UT a correlated wind response was observed between region C and the Davis zenith; however, region A (and region B after ~17:10 UT) observed vertical winds of opposite sign to those in the poleward regions. As such a strongly anticorrelated wind response was observed between regions C and A, a baseline of ~300 km. Spatially

isolated upward winds were later observed above Davis and in regions C and B, while a spatially large-scale upward wind was observed above Davis and in all three common volume regions between 22:10 and 23:45 UT, associated with very low auroral brightness on the poleward edge of the auroral oval. *Innis et al.* [1999] reported an event during which an upward wind of $\geq$100 m s^{-1} was first observed above Davis station and then above Mawson approximately 1 h later, at which time the upward motion above Davis was still very strong (~200 m s^{-1}). This event was observed in the same time sector as the large-scale upward wind reported in the current study (22:00–24:00 UT).

[39] The larger high-frequency variability observed in the vertical winds above Mawson compared to those in the common volume regions (and probably above Davis, although the lower time resolution of the Davis data makes this difficult to quantify) was noteworthy. One possible contributor to this increased variability may be due to a time-varying background level in the images recorded by the EMCCD camera in use at Mawson. The airglow signal is superimposed on a large background due to the camera (and therefore not associated with continuum airglow emission), and if this background varied during an etalon scan (as has been observed with a similar camera in Alaska) it could introduce spectral distortion. The central zone is the most sensitive to this type of distortion because it spans a very small range of spectral phase, and thus large frame-to-frame signal variations do not get distributed across many spectral channels as is the case with zones farther from the optical axis. The net result would be increased uncertainty in the central zone spectral fits and greater variability (of instrumental origin) in the vertical wind. Another factor which certainly would have contributed to the difference in variability is simply the fact that the region A and B line-of-sight winds were each averaged over two zones (see Table 1), which helped to suppress uncorrelated variability. In region C the Mawson SDI was least sensitive to the vertical wind component due to the greater zenith angle, which also resulted in less high-frequency variability in that region.

[40] The discussion of spatial correlation is complicated by the possible contribution to spatial variations from atmospheric gravity waves (AGW), which can have wavelengths ranging from 100's to 1000's of kilometers [e.g., *Hunsucker*, 1982]. *Innis and Conde* [2002] inferred maps of vertical wind variability from Dynamics Explorer 2 data and showed that the region of high vertical wind variability was predominantly bounded by the (statistical) location of the auroral oval. These maps were interpreted as a possible signature of polar cap gravity waves, and, comparing these maps to the locations of Mawson and Davis stations, it is apparent that both would be located within the region of increased wave activity, particularly in the postmagnetic midnight sector.

[41] Other investigators have observed varying degrees of correlation between spatially separated vertical wind measurements. *Kosch et al.* [2000] for example observed essentially no correlation between vertical winds over a 45 km baseline, at both E and F region altitudes. On the other hand *Ishii et al.* [2004] observed good correlation in E region vertical winds over an approximately 300 km baseline, with somewhat poorer correlation in the F region. The spatial extent of vertical motion will naturally depend on the driving forces which are acting. Spatially localized impulsive heating events, for example, associated with auroral precipitation and/or locally enhanced Joule heating (common during substorms [e.g., *Chun et al.*, 2002; *Østgaard et al.*, 2002]), may drive strong vertical winds in the upper thermosphere which are confined to relatively small horizontal areas. Large-scale driving forces, possibly associated with quasi-stationary (in a Sun-aligned coordinate system) sources of heating or divergent/convergent ion motion, might be expected to produce a similarly large-scale vertical wind response.

[42] Indeed, the large-scale upward wind between 22:10 and 23:45 UT was observed in conjunction with relatively strong divergence in the wind field inferred by the Mawson SDI. The divergence estimate displayed in Figure 9 is an all-sky average value returned by the vector fitting algorithm; however, the large-scale nature of the observed vertical wind disturbance (it was observed in all regions except above Mawson) makes it appropriate to compare with the (field-of-view average) horizontal divergence, and at least in this sense the directions of the vertical wind and the sign of the divergence were in agreement with the approximate relationship given by *Burnside et al.* [1981], namely,

$$w = H\left(\frac{\partial u}{\partial x} + \frac{\partial v}{\partial y}\right) \tag{5}$$

where w, u, and v are the vertical, zonal, and meridional wind speed, respectively; H is the scale height; and the partial derivatives are with respect to the zonal (x) and meridional (y) distance. Equation (5) would be expected to hold when the time rate of change of pressure at the level of the airglow emission is negligibly small, the horizontal velocity components are constant with height, the atmosphere is isothermal above the level of the airglow, and horizontal gradients in atmospheric density are negligible.

[43] To test the ability of equation (5) to model the vertical wind/divergence relationship, consider Figure 10. For both days considered in this study, every measured vertical wind (in each of the common volume regions and in the station zeniths) was associated with a divergence estimated from the Mawson SDI (linearly interpolated to the times at which the vertical wind measurements were made). The vertical winds were then sorted into divergence bins of width 5×10^{-5} s^{-1}, and the mean vertical wind within each divergence bin calculated. These average vertical winds are plotted in Figure 10, red triangles for day 99 and blue squares for day 98, with the 1σ deviation within each divergence bin displayed as an error bar for each plotting symbol. The solid black line shows the trend which would be expected from equation (5), using a scale height estimated using the NRLMSISE-00 empirical model [*Picone et al.*, 2002], driven by geomagnetic and solar activity inputs, in addition to the all-sky average temperature measured by the Mawson SDI (for an altitude of 240 km, the assumed altitude of the airglow emission peak). Only one modeled line is shown as the scale heights for both nights were very similar, at approximately 34 km.

[44] Clearly there was significant scatter in the underlying vertical winds relative to the divergence (shown by the size

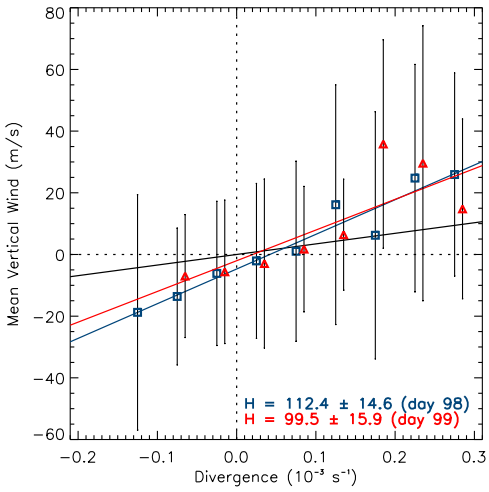

Figure 10. Average vertical winds from all regions plotted against (all-sky average) divergence calculated from the Mawson SDI wind fields. Symbols show average vertical wind (red triangles for day 99, blue squares for day 98) within divergence bins of width 5×10^{-5} s^{-1}. The solid black line indicates the trend expected from equation (5) for a scale height of 34 km.

of the error bars), and this was exacerbated by the fact that the divergence was essentially an average across the Mawson SDI field of view (and was interpolated in time to match the vertical wind measurements) and thus would not always reflect the divergence occurring within smaller regions centered on the vertical wind measurements. However, it is also likely that the large scatter indicates that the assumptions underlying equation (5) can be, and often are (at least locally), violated. In an average sense however, the relation given by Burnside modeled the observed vertical winds moderately well (when enough data points were contained in a divergence bin), in that it predicted a linear trend and associated positive divergence with upward winds; however, the scale heights calculated from this data set were much higher than the modeled value of 34 km. Straight-line fits to the data (shown in Figure 10 by the solid red and blue lines for days 99 and 98, respectively, with calculated scale heights shown in the bottom-right corner of the plot) indicated scale heights approximately 3–4 times greater than the modeled value on both nights; however, this may have been in part attributable to the large scatter at the upper end of the divergence range which was observed on both nights. It is also quite possible that the local divergence (in a smaller region centered on the wind measurement) at any given time was higher than the average value determined from the fitted wind field, which would act to reduce the calculated scale height. Note also that the data appeared to be slightly biased toward downward vertical winds (hence the fitted lines did not pass directly through the origin) when divergence was small, which is most likely a consequence of the limited amount of data.

[45] Similar comparisons between measured vertical winds and divergence have been carried out by other authors. *Biondi* [1984] reported upward vertical motions at midlatitudes associated with positive horizontal divergence and downward vertical winds associated with convergence; however, the observed vertical motions were larger than would be expected from the Burnside relation, in agreement with the present study. *Smith and Hernandez* [1995] observed the opposite trend (upward vertical winds associated with negative divergence, and vice versa) on one very active night during a storm period, at South Pole station, which is at a similar magnetic latitude to Davis. These authors attributed the opposite sense of the data to divergent horizontal flow being the driving force for the vertical wind, and obtained a value for the scale height of −78.8 km, comparable in magnitude to the values calculated in the present study. *Guo and McEwen* [2003] performed a similar comparison in the Northern Hemisphere and observed a similar trend to that shown in Figure 10.

[46] *Cooper et al.* [2009] tested the validity of equation (5) using a local-scale, time-dependent, three-dimensional model of the neutral atmosphere and found that it was generally only applicable above the height of maximum energy and momentum deposition per unit mass, and at times when the forcing did not change rapidly with time. Below the height of maximum forcing the Burnside condition predicted the incorrect sign for the vertical wind. Given these findings it is possible that the discrepancies between modeled (via equation (5)) and measured vertical winds in the present work and those cited above are at least partly attributable to either rapidly time-varying energy/momentum inputs or variable deposition heights.

6. Conclusion

[47] Results have been presented from a bistatic experiment utilizing Fabry-Perot spectrometers at Mawson and Davis stations. Vertical winds were calculated at three locations along the great circle joining Mawson and Davis stations, in addition to the vertical winds routinely observed above each station, and the time evolution of the vertical wind at these locations has been examined. Clear association was observed between vertical wind disturbance and the presence of active aurora, and correlation between the vertical wind response at separate locations was observed on a range of spatial scales from ~150–480 km.

[48] The general behavior of the observed vertical winds was in agreement with earlier studies; namely, upward vertical winds were observed poleward of auroral arcs and sustained (though weak) downward winds were observed early in the night. A strong vertical wind disturbance on 7 April 2008 was seen to be linked to large gradients in the horizontal wind field associated with the motion of an auroral arc. Comparison between vertical winds and the all-sky average horizontal divergence showed that the Burnside relation (equation (5)) modeled the average behavior moderately well; however, scale heights approximately 3–4 times larger than the modeled value (at 240 km altitude) on both nights are required to better explain the data.

[49] While the current set of bistatic measurements is small, owing to the need for clear skies above and between both stations, monitoring the time evolution of the vertical wind field at multiple locations is an important technique for the study of gravity waves, considered to be a ubiquitous feature of the upper atmosphere at auroral latitudes. Future

studies will aim to characterize these waves and their relationship to auroral energy inputs.

[50] **Acknowledgments.** This research has been supported by the Australian Research Council's Discovery Project DP0557369 and by the Australian Antarctic Science Program. Logistic support for this work was provided by the Australian Antarctic Division. The NRLMSISE-00 model is provided by the Community Coordinated Modeling Center (CCMC). IMF data are supported by the NASA/ACE program. The authors wish to acknowledge the continuing support of the ANARE expeditioners at Mawson and Davis stations, without which this work would not have been possible.

[51] Robert Lysak thanks Gary Swenson and another reviewer for their assistance in evaluating this manuscript.

References

Anderson, C., M. Conde, P. Dyson, T. Davies, and M. J. Kosch (2009), Thermospheric winds and temperatures above Mawson, Antarctica, observed with an all-sky imaging, Fabry-Perot spectrometer, *Ann. Geophys.*, *27*, 2225–2235.

Aruliah, A. L., and D. Rees (1995), The trouble with thermospheric vertical winds: geomagnetic, seasonal and solar cycle dependence at high latitudes, *J. Atmos. Terr. Phys.*, *57*(6), 597–609.

Aruliah, A. L., E. M. Griffin, I. McWhirter, A. D. Aylward, E. A. K. Ford, A. Charalambous, M. J. Kosch, C. J. Davis, and V. S. C. Howells (2004), First tristatic studies of meso-scale ion-neutral dynamics and energetics in the hight-latitude upper atmosphere using collocated FPIs and EISCAT radar, *Geophys. Res. Lett.*, *31*, L03802, doi:10.1029/2003GL018469.

Aruliah, A. L., et al. (2005), First direct evidence of meso-scale variability on ion-neutral dynamics using co-located tristatic FPIs and EISCAT radar in Northern Scandinavia, *Ann. Geophys.*, *23*, 147–162.

Biondi, M. A. (1984), Measured vertical motion and converging and diverging horizontal flow of the midlatitude thermosphere, *Geophys. Res. Lett.*, *11*, 84–87.

Burnside, R. G., F. A. Herrero, J. W. Meriwether Jr., and J. C. G. Walker (1981), Optical observations of thermospheric dynamics at Arecibo, *J. Geophys. Res.*, *86*, 5532–5540.

Chun, F. K., D. J. Knipp, M. G. McHarg, J. R. Lacey, G. Lu, and B. A. Emery (2002), Joule heating patterns as a function of polar cap index, *J. Geophys. Res.*, *107*(A7), 1119, doi:10.1029/2001JA000246.

Conde, M. (2001), Analysis of Fabry-Perot spectra of lidar backscatter echoes, in *ANARE Reports*, vol. 146, edited by R. J. Morris and P. J. Wilkinson, pp. 91–114, Aust. Antarct. Div., Kingston, Tasmania, Australia.

Conde, M. (2002), Deriving wavelength spectra from fringe images from a fixed-gap single-etalon Fabry-Perot spectrometer, *Appl. Opt.*, *41*, 2672–2678.

Conde, M., and P. L. Dyson (1995a), Thermospheric horizontal winds above Mawson, Antarctica, *Adv. Space Res.*, *16*(5), 41–52.

Conde, M., and P. L. Dyson (1995b), Thermospheric vertical winds above Mawson, Antarctica, *J. Atmos. Terr. Phys.*, *57*(6), 589–596.

Conde, M., and R. W. Smith (1997), 'Phase compensation' of a separation scanned, all-sky imaging Fabry-Perot spectrometer for auroral studies, *Appl. Opt.*, *36*, 5441–5450.

Conde, M., and R. W. Smith (1998), Spatial structure in the thermospheric horizontal wind above Poker Flat, Alaska, during solar minimum, *J. Geophys. Res.*, *103*, 9449–9472.

Cooper, S. L., M. Conde, and P. Dyson (2009), Numerical simulations of thermospheric dynamics: divergence as a proxy for vertical winds, *Ann. Geophys.*, *27*, 2491–2502.

Greet, P. A., M. G. Conde, P. L. Dyson, J. L. Innis, A. M. Breed, and D. J. Murphy (1999), Thermospheric wind field over Mawson and Davis, Antarctica; simultaneous observations by two Fabry-Perot spectrometers of λ630 nm emission, *J. Atmos. Sol. Terr. Phys.*, *61*(146), 1025–1045.

Greet, P. A., J. L. Innis, and P. L. Dyson (2002), Thermospheric vertical winds in the auroral oval/polar cap region, *Ann. Geophys.*, *20*, 1987–2001.

Guo, W., and D. J. McEwen (2003), Vertical winds in the central polar cap, *Geophys. Res. Lett.*, *30*(14), 1725, doi:10.1029/2003GL017124.

Hunsucker, R. D. (1982), Atmospheric gravity waves generated in the high-latitude ionosphere: A review, *Rev. Geophys.*, *20*, 293–513.

Innis, J. L., and M. Conde (2002), High-latitude thermospheric vertical wind activity from Dynamics Explorer 2 wind and temperature observations: Indications of a source region for polar cap gravity waves, *J. Geophys. Res.*, *107*(A8), 1172, doi:10.1029/2001JA009130.

Innis, J. L., P. A. Greet, and P. L. Dyson (1996), Fabry-Perot spectrometer observations of the auroral oval/polar cap boundary above Mawson, Antarctica, *J. Atmos. Terr. Phys.*, *58*(16), 1973–1988.

Innis, J. L., P. A. Greet, D. J. Murphy, M. G. Conde, and P. L. Dyson (1999), A large vertical wind in the thermosphere at the auroral oval/polar cap boundary seen simultaneously from Mawson and Davis, Antarctica, *J. Atmos. Sol. Terr. Phys.*, *61*, 1047–1058.

Ishii, M. (2005), Relationship between thermospheric vertical wind and the location of ionospheric current in the polar region, *Adv. Polar Upper Atmos. Res.*, *19*, 63–70.

Ishii, M., M. Conde, R. W. Smith, M. Krynicki, E. Sagawa, and S. Watari (2001), Vertical wind observations with two Fabry-Perot interferometers at Poker Flat, Alaska, *J. Geophys. Res.*, *106*, 10,537–10,551.

Ishii, M., M. Kubota, M. Conde, R. W. Smith, and M. Krynicki (2004), Vertical wind distribution in the polar thermosphere during Horizontal *E* Region Experiment (HEX) campaign, *J. Geophys. Res.*, *109*, A12311, doi:10.1029/2004JA010657.

Jones, N., P. Wardill, and F. Jacka (1987), Dynamics of the thermosphere over Mawson, Antarctica: II. Dependence on the Y component of the interplanetary magnetic field, in *ANARE Research Notes*, vol. 48, edited by G. B. Burns and M. Craven, pp. 121–130, Aust. Antarct. Div., Kingston, Tasmania, Australia.

Kosch, M. J., M. Ishii, A. Kohsiek, D. Rees, K. Schlegel, T. Hagfors, and K. Cierpka (2000), A comparison of vertical thermospheric winds from Fabry-Perot interferometer measurements over a 50 km baseline, *Adv. Space Res.*, *26*(6), 985–988.

Østgaard, N., R. R. Vondrak, J. W. Gjerloev, and G. Germany (2002), A relation between the energy deposition by electron precipitation and geomagnetic indices during substorms, *J. Geophys. Res.*, *107*(A9), 1246, doi:10.1029/2001JA002003.

Picone, J. M., A. E. Hedin, D. P. Drob, and A. C. Aikin (2002), NRLMSISE-00 empirical model of the atmosphere: Statistical comparisons and scientific issues, *J. Geophys. Res.*, *107*(A12), 1468, doi:10.1029/2002JA009430.

Price, G. D., R. W. Smith, and G. Hernandez (1995), Simultaneous measurements of large vertical winds in the upper and lower thermosphere, *J. Atmos. Terr. Phys.*, *57*(6), 631–643.

Rees, D., R. W. Smith, P. J. Charleton, N. McCormac, F. G. abd Lloyd, and Åke Steen (1984), The generation of vertical winds and gravity waves at auroral latitudes - i. Observations of vertical winds, *Planet. Space Sci.*, *32*(6), 667–684.

Rishbeth, H., T. J. Fuller-Rowell, and D. Rees (1987), Diffusive equilibrium and vertical motion in the thermosphere during a severe magnetic storm: a computational study, *Planet. Space Sci.*, *35*(9), 1157–1165.

Sipler, D. P., M. A. Biondi, and M. E. Zipf (1995), Vertical winds in the midlatitude thermosphere from Fabry-Perot Interferometer measurements, *J. Atmos. Terr. Phys.*, *57*(6), 621–629.

Smith, R. W. (1998), Vertical winds: A tutorial, *J. Atmos. Sol. Terr. Phys.*, *60*, 1425–1434.

Smith, R. W. (2000), The global-scale effect of small-scale thermospheric disturbances, *J. Atmos. Sol. Terr. Phys.*, *62*, 1623–1628.

Smith, R. W., and G. Hernandez (1995), Vertical winds in the thermosphere within the polar cap, *J. Atmos. Terr. Phys.*, *57*(6), 611–620.

Smith, R. W., G. Hernandez, R. G. Roble, P. L. Dyson, M. Conde, R. Crickmore, and M. Jarvis (1998), Observation and simulations of winds and temperatures in the Antarctic thermosphere for August 2–10, 1992, *J. Geophys. Res.*, *103*, 9473–9480.

Spencer, N. W., L. E. Wharton, H. B. Niemann, A. E. Hedin, G. R. Carignan, and J. C. Maurer (1981), The Dynamics Explorer wind and temperature spectrometer, *Space Sci. Instrument.*, *5*, 417–428.

Spencer, L. E. Wharton, G. R. Carignan, and J. C. Maurer (1982), Thermosphere zonal winds, vertical motions and temperature as measured from Dynamics Explorer, *Geophys. Res. Lett.*, *9*, 953–956.

Wardill, P., and F. Jacka (1986), Vertical motions in the thermosphere over Mawson, Antarctica, *J. Atmos. Terr. Phys.*, *48*(3), 289–292.

C. Anderson and M. Conde, Geophysical Institute, University of Alaska Fairbanks, PO Box 757320, Fairbanks, AK 99775, USA. (callum@gi.alaska.edu)

T. Davies and P. L. Dyson, Department of Physics, La Trobe University, Melbourne, Vic 3086, Australia.

M. J. Kosch, Department of Physics, Lancaster University, Infolab21, South Drive, Lancaster LA1 4YB, UK.